Fluorogenic Reaction Probes Defect Sites on Titanium Dioxide Nanoparticles

Li Zuo^{[a][b] Δ}, Mohammad Akter Hossain^{[a] Δ}, Rabindra Dubadi^[a], Madelyn M. Kist^[a], Fatiha Farhana^[a], Jiao Chen^[a], Mietek Jaroniec^[a], Hao Shen^{[a]*}

[∆]These authors contributed equally.

[a] Li Zuo, Mohammad Akter Hossain, Rabindra Dubadi, Madelyn M. Kist, Fatiha Farhana, Mietek Jaroniec, Hao Shen

Department of Chemistry and Biochemistry

Kent State University

800 E. Summit St., Kent, Ohio, 44242, USA

E-mail: hshen7@kent.edu

[b] Li Zuc

School of Chemistry and Chemical Engineering

Naniing University

163 Xianlin Road, Nanjing, Jiangsu, 210023, China

Abstract: Titanium dioxide nanoparticles (TiO2 NPs) have traditionally been utilized as industrial catalysts, finding widespread application in various chemical processes due to their exceptional stability and minimal toxicity. However, quantitatively assessing the reactive sites on TiO2 NPs remains a challenge. In this study, we employed a fluorogenic reaction to probe the apparent reactivity of TiO₂ NPs. By manipulating the number of defect sites through control of hydrolysis speed and annealing temperature, we determined that the Ti(III) content is positively correlated with the reactivity of TiO2 NPs. Additionally, these Ti(III) sites could be introduced by reducing commercial TiO2 NPs using NaBH4. Our findings suggest that fluorogenic oxidation of Amplex Red is an effective method for probing defect site densities on TiO2 NPs. Utilizing single-molecule fluorescence imaging, we demonstrated the ability to map defect site density within TiO2 nanowires. Achieving sub-nanoparticle spatial resolution, we observed significant intraparticle and interparticle variations in the defect site distribution, leading to substantial reactivity heterogeneity.

Introduction

 ${\rm TiO_2}$ NPs have attracted significant attention owing to their distinctive properties, including exceptional chemical stability, high catalytic efficiency, eco-friendliness, and facile synthesis ¹⁻³. Since the original work by Fujishima and Honda, who pioneered the photochemical hydrogen production on ${\rm TiO_2}^{4, 5}$, ${\rm TiO_2}$ NPs

have found widespread utility as catalysts in energy conversion and pollutant remova⁶⁻⁹. In contrast to the bulk phase TiO₂, the catalytic performance of TiO₂ NPs is highly dependent on their surface structure. It has become a common practice to control the size of catalytic NPs to optimize the surface-to-volume ratio and manipulate the NP shape to introduce distinct facets and coordination patterns of central atoms for catalytic applications^{3, 10-15}. To further enhance the catalytic performance, it is crucial to elucidate the chemical nature of reactive sites on TiO₂ NPs and pinpoint the distributions of the reactive sites on TiO₂ NPs.

Considerable efforts have been made to the exploration of the physical and chemical properties of TiO₂¹⁶⁻¹⁸. Recent studies have revealed that the reactivity is facet-dependent. Furthermore, researchers discovered that O-Ti-O centers with lower coordination numbers exhibit the highest catalytic reactivity, especially in oxidative reactions^{9, 17, 19, 20}. These low-coordination Ti centers are known as defect sites due to their unsaturated bonding. The oxygen vacancies are the most important form of all defect sites because they exist widely in all kinds of TiO₂ NPs. It was confirmed experimentally and theoretically that the oxygen vacancies can directly affect adsorption and activation during heterogeneous catalysis^{17, 19, 21, 22}.

The oxygen vacancies play a pivotal role in catalyzing transformations of O_2 , H_2O , or H_2O_2 into diverse reactive oxygen species (ROS), which serve as crucial intermediates during these processes. Notably, the oxidation efficiency of ROS significantly surpasses that of their parent oxidants. For instance, Lu et al.

found that ${}^{\bullet}O_2{}^{-}$ radicals were generated on highly dispersed TiO₂ NPs in the presence of H₂O₂. These oxygen vacancies acted as the primary active sites for the oxidative desulfurization of dibenzothiophene (DBT) ²³. Sánchez et al. reported the catalytic degradation of methylene blue by TiO₂ NPs where both ${}^{\bullet}OH$ and HOO ${}^{\bullet}$ radicals were generated on oxygen vacancies²⁴. It is generally believed that the defect sites on TiO₂ NPs would govern the overall catalytic reactivity. However, it is unclear how these defect sites would be distributed along the TiO₂ NPs because conventional methods do not offer information on subnanoparticle activities. Single-molecule fluorescence imaging is the solution to this obstacle, since it offers unprecedented spatiotemporal resolution for heterogeneous catalysis.

In this work, we discovered that the N-deacetylation oxidation of Amplex Red (AR) is converted to a highly fluorescent molecule resorufin (RF) at the Ti(III) centers. Previously, AR was used as a probe in photochemical catalysis to map out the hole distributions²⁵⁻²⁸. We found that in the presence of H₂O₂, the amplex conversion on TiO₂ samples is directly proportional to the number of Ti(III) centers. Through thermal annealing and chemical reduction, we were able to adjust the number of reactive sites on both commercial and homemade titania NPs. Furthermore, we discovered that the •OH and •O₂⁻ radicals were generated at the reactive sites which are responsible for the apparent reactivity. By harnessing the power of single-molecule fluorescence microscopy and super-resolution imaging, we demonstrated that such a fluorogenic reaction can effectively map

out the defect site distribution within a single TiO_2 nanowire (TiO_2 NW), a typical 1D structural material. The fluorogenic reaction in combination with the single-molecule fluorescence approach offers a rapid and straightforward way to evaluate structural properties of TiO_2 NP at the sub-nanoparticle level.

Results and Discussion

To explore the role of defects in catalysis, we utilized two distinct TiO₂ samples: the commercial TiO₂ (C-TiO₂) and the homemade TiO₂ (HM-TiO₂-2.5-110). The C-TiO₂, a blend of rutile/anatase phases, underwent thermal annealing at 900°C, according to the manufacturer, to eliminate defect sites. Conversely, HM-TiO₂-2.5-110 was produced via a hydrothermal method without subsequent annealing, leading us to anticipate a high defect content. During synthesis, we noted the solution's color transitioned to light blue following initial hydrolysis ($TiCl_3 + H_2O \rightarrow Ti(OH)(OH_2)_5^{2+}$), suggestive of Ti(III) formation. These Ti(III) oxidized only partially into TiO2, resulting in a sample rich in Ti(III) defect sites. The transmission electron microscopy (TEM) images of HM-TiO₂-2.5-110 revealed a distinct lattice plane distance of 0.32 nm, aligning with the (1 1 0) lattice plane of rutile TiO2. The structural characteristics were further examined by X-ray diffraction (XRD) patterns, detailed in the Supporting Information Fig. S3.

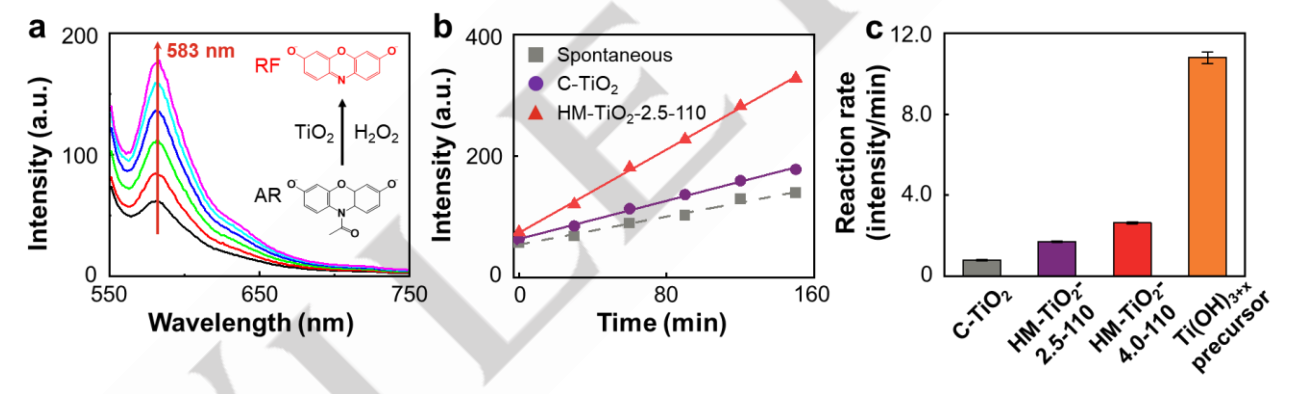


Figure 1. Catalytic performance of C-TiO₂ and HM-TiO₂. (a) Time-dependent fluorescence spectra of AR oxidation catalyzed by C-TiO₂. The spectrum curves were collected every 30 min. Excitation wavelength = 532 nm. (b) The fluorescence intensities at 583 nm versus time from the measurements on C-TiO₂ and HM-TiO₂-2.5-110. (c) Catalytic reaction rates comparison between C-TiO₂, HM-TiO₂ and Ti(OH)_{3+x} precursor[#]. HM-TiO₂-pH-T represents the sample prepared at corresponding pH and annealed at T°C. #: Ti(OH)_{3+x} precursor (light blue suspension) was formed when the hydrothermal of TiCl₃ solution had been processed for ~3 h. Reaction conditions: [AR] = 19.4 μ M, [H₂O₂] = 60 mM, [TiO₂] = 0.5 mg mL⁻¹. All experiments were performed in a 5 mM pH 7.4 phosphate buffer. The spontaneous reaction (grey dash line) is shown as a comparison.

We used the oxidation of AR as a probe reaction to determine the reactivity of TiO_2 NPs. AR transforms into a highly fluorescent molecule, RF, in the presence of hydrogen peroxide (H_2O_2) and a catalyst. As depicted in **Fig. 1a**, there was an escalation in the fluorescence intensity during product formation. The peak intensity at approximately 583 nm demonstrates a linear dependence on the reaction duration, indicative of pseudo-zero order reaction kinetics. Typically, AR oxidation is regarded as a pseudo-first order reaction^{25, 29}. The linear increase in the RF

concentration at 30-minute intervals is likely attributable to the relatively slow reaction rate (**Fig. 1b**). Consequently, we determined the slope of each time-dependent trajectory to quantify the reactivity for each TiO_2 NP. We observed that C-TiO₂ displayed a reactivity of approximately 0.2 min^{-1} mg⁻¹ (**Fig. 1c**). In comparison to the 30 nm gold nanoparticle (AuNP), a catalyst previously analyzed for the same AR oxidation, the reactivity of C-TiO₂ is 36 times inferior (**Fig. S5b**). Therefore, C-TiO₂ exhibits negligible activity for AR oxidation.

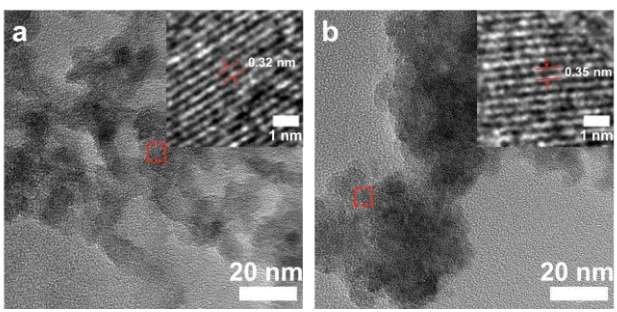


Figure 2. TEM images of HM-TiO₂-2.5-110 (a) and HM-TiO₂-4.0-110 (b). Insets: high resolution TEM images of the region boxed in (a) and (b), the corresponding lattice distance is measured for each image.

Surprisingly, the HM-TiO $_2$ -2.5-110 sample exhibited twofold higher reactivity than C-TiO $_2$. The reactivity variation between C-TiO $_2$ and HM-TiO $_2$ -2.5-110 is attributed to the amount of Ti(III) defect sites present in these samples. To investigate the role of Ti(III) defects in catalysis, we synthesized the homemade HM-TiO $_2$ -4.0-110 sample by elevating the pH value to 4.0 during TiCl $_3$ hydrolysis. The increased pH value favors more rapid TiCl $_3$ hydrolysis, creating more Ti(III) defects in the resulting HM-TiO $_2$ -4.0-110. As expected, HM-TiO $_2$ -4.0-110 displayed reactivity 1.5 times higher than that of HM-TiO $_2$ -2.5-110. This result further

suggests that defect sites are responsible for the chemical reactivity, and the hydrolysis rate is the key to defect site formation. In particular, we measured the reactivity of the light blue sol precursor, a hydrolyzed TiCl₃ solution, in catalyzing AR oxidation. This precursor exhibited approximately tenfold higher reactivity compared to C-TiO2 (Fig. 1c). This extremely high reactivity can be attributed to two compounds present in the precursor solution: Ti3+ ions in the form of soluble Ti(III)complexes and fine particles of Ti(III)-Ti(IV)-based double oxide, the Magnéli's phase 30-32. Magnéli's phase is known for its high density of surface defects and elevated surface potential, which could account for its remarkable catalytic reactivity. Notably, HM-TiO₂ NPs precipitated at pH 2.5 exhibited a rod-like morphology, while those precipitated at pH 4.0 exhibited clear morphological changes. The average particle size was estimated to be approximately 6 nm for HM-TiO₂-2.5-110 and 5 nm for HM-TiO₂-4.0-110. High-resolution TEM images (Fig. 2a, inset) revealed that HM-TiO₂-2.5-110 exhibited a clear lattice plane distance of 0.32 nm, corresponding to the (1 1 0) lattice plane of rutile TiO₂. In contrast, HM-TiO2-4.0-110 displayed a lattice distance of 0.35 nm (Fig. 2b, inset), corresponding to the (1 0 1) plane of anatase TiO₂. These findings suggest that the Ti(III) defects could alter the morphology of TiO₂ in addition to influencing chemical reactivity.

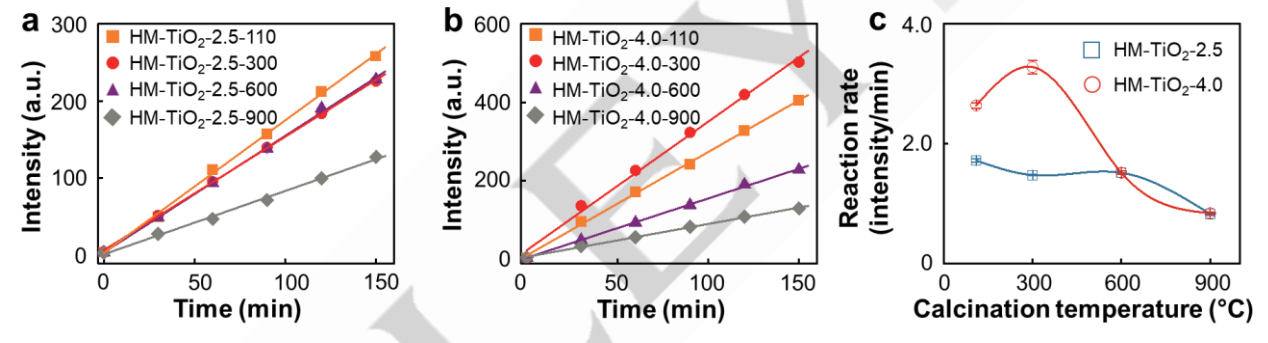


Figure 3. Modulation of the catalytic performance on HM-TiO₂. (a, b) Annealing temperature dependence on the catalytic reactivity of HM-TiO₂ prepared at pH 2.5 (a) and 4.0 (b). (c) Catalytic reaction rates versus annealing temperature from (a) and (b). HM-TiO₂-pH-T represents the sample prepared at the corresponding pH and annealed at T°C. All reactions were performed with 19.4 μ M AR, 60 mM H₂O₂ and 0.5 mg mL⁻¹ HM-TiO₂ at 5 mM pH 7.4 phosphate buffer. The reaction rates were calculated from the linear fitting in (a) and (b).

To mimic C-TiO₂ and determine the role of thermal annealing, we annealed the HM-TiO₂-2.5 and HM-TiO₂-4.0 samples at 300°C, 600°C, and 900°C for 12 hours, respectively. The corresponding samples are annotated with their treatment temperatures (Fig. 3a and b). Remarkably, the impact of annealing temperature on reactivity exhibited distinct behaviors for HM-TiO2-2.5 and HM-TiO₂-4.0, as depicted in Fig. 3c. For HM-TiO₂-2.5, its reactivity decreased with increasing annealing temperature. Other than the oxidation of Ti(III) defects, several additional factors also contributed to the decreased reactivity. These factors include the particle shape shift (Fig. S3d and e) and particle size increase from 5.0 to 7.2 nm (Table S1). Conversely, annealing at 300°C resulted in an approximate 25% increase in reactivity for HM-TiO₂-4.0. It was found that there was a slight increase in the particle size from 4.9 to 5.6 nm, and the Magnéli TiO2 phase became the dominant form after this annealing step (Fig. S4).

This emergence of Magnéli's phase may account for the observed increase in reactivity. Upon annealing at 600° C, the reactivity of HM-TiO₂-2.5 remained relatively stable, suggesting that the rutile phase is relatively stable within the temperature range of 300 to 600° C. Conversely, for HM-TiO₂-4.0, the reactivity experienced a sharp decline due to a crystal phase transformation from anatase to rutile. At the highest temperature of 900° C, particle sintering occurred in both HM-TiO₂ NPs, resulting in the formation of larger particles, approximately 60 nm in size, and a subsequent decrease in reactivity. This drop in reactivity brought it in line with that of C-TiO₂, as expected.

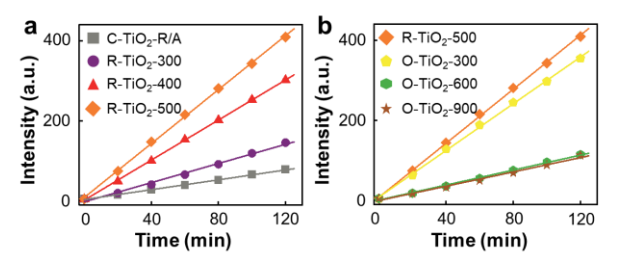


Figure 4. Reversible catalytic reactivity of C-TiO₂ for the AR oxidation. (a) Reactivity measurements of the reduced C-TiO₂ (presented as R-TiO₂-T, T for reduction temperature). (b) Reactivity measurements of the re-oxidized R-TiO₂-500 annealed at different temperatures (presented as O-TiO₂-T, T for annealing temperature). Reaction conditions: [AR] = 19.4 μ M, [H₂O₂] = 60 mM, [TiO₂] = 0.5 mg mL⁻¹. All experiments were performed at 5 mM pH 7.4 phosphate buffer.

To gain further insight into the pivotal role of low-valence titanium Ti(III) as defect sites in catalytic enhancement, we employed a reduction process involving the use of NaBH4 under a nitrogen atmosphere to prepare reduced TiO2 (R-TiO2). The clear color change from white to deep blue-black indicated the introduction of Ti(III) centers by forming TiO_{2-x}³³⁻³⁵. We systematically investigated the relationship between reduction temperature and reactivity, as illustrated in Fig. 4a. Interestingly, we observed that as the reduction temperature increased, the reactivity exhibited a corresponding increase. Notably, R-TiO₂-500 displayed approximately six times higher reactivity than the parent C-TiO₂ for AR oxidation. This observation clearly associates the existence of oxygen vacancies to defect sites on TiO2 NPs, which greatly impacts their catalytic reactivity. Moreover, we conducted a reverse oxidation process on R-TiO₂-500 under air at varying temperatures. As depicted in Fig. 4b, the reactivity decreased following the oxidation in air. It is worth noting that the abrupt disappearance of reactivity enhancement after annealing at 600°C provided a valuable insight into the crystal transition and annealing temperature, which can be leveraged in catalyst design. The blue powder reverted to its original white color, signifying the complete oxidation of TiO_{2-x}.

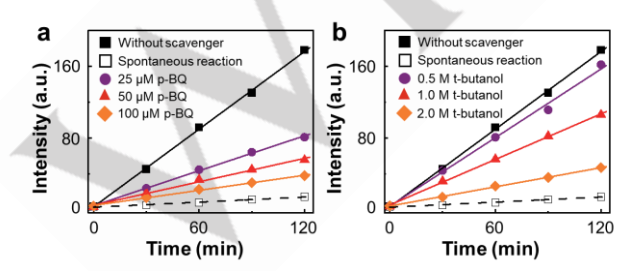
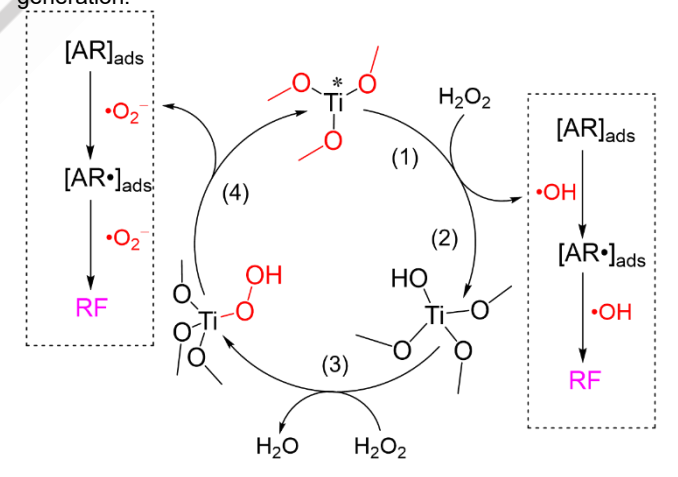


Figure 5. Radical trapping experiments for AR oxidation catalyzed by HM-TiO₂-4.0-110. (a) Trapping experiments of ${}^{\bullet}O_2^{-}$ by using p-BQ as the superoxide radical scavenger. (b) Trapping experiments of ${}^{\bullet}OH$ by using t-butanol as the hydroxyl radical scavenger. Reaction conditions: [AR] = 9.7 μ M, [H₂O₂] = 20 mM, [TiO₂] = 0.5 mg mL⁻¹. All experiments were performed at 5 mM pH 7.4 phosphate buffer.

It is important to note that there are typically two types of ROS, •O₂ and •OH radicals on the surface of TiO₂ NPs during catalytic transformations. To identify which of these radicals were primarily produced during the catalysis, we conducted radical scavenging experiments using p-benzoquinone (p-BQ) and tert-butanol (tbutanol) as •O₂⁻ and •OH scavengers^{36, 37} (**Fig. 5**), respectively. Our observations revealed that the reactivity of AR oxidation on HM-TiO₂ NPs was significantly influenced by the concentration of p-BQ and t-butanol, indicating the coexistence of •OH and •O2radicals. In the presence of H₂O₂, the reductive activation of H₂O₂ by transition metal ions is known to generate •OH as an intermediate radical species. Notably, Ti³⁺ is widely recognized as an inorganic reductant due to its exceptional electron-donating properties^{2, 7, 19, 38}. The one-electron redox reaction between Ti³⁺ and H_2O_2 proceeds rapidly and follows the well-established Fenton mechanism^{39, 40}. However, in heterogeneous catalysis, catalytic reactions predominantly occur on the surface of catalysts, and the activation of H₂O₂ on solid catalysts is significantly influenced by their chemical composition, elemental valence, crystal structure, and surface state9, 17, 19, 21, 34. In this study, the presence of low-valence Ti(III) species enabled the defective lattice ≡Ti(III) to serve as reactive sites for the Fenton-like reaction. Based on these results, we propose a plausible mechanism for the generation of ROS (Scheme 1). Such a mechanism is distinctively different from previous studies in which AR was employed to evaluate the photochemical reactivity of semiconducting nanostructures^{26, 41-47} Others' previous studies used AR under UV excitation, and without the presence of H₂O₂; thus, the reaction is considered a hole probe without the formation of ROS at the defect centers.

Scheme 1. The proposed Fenton-like mechanism for ROS generation.



Several reaction steps are involved in the proposed reaction cycle: (1) H_2O_2 adsorbs onto the defective $\equiv Ti(III)$ sites (indicated by *) with a high adsorption energy, resulting in the formation of $\equiv Ti(III)$ – $H_2O_2^{48, 49}$. (2) The adsorbed H_2O_2 becomes activated, leading to the elongation and eventual cleavage of the O–O bond. This cleavage generates *OH radicals and $\equiv Ti(IV)$ –OH species⁵⁰⁻⁵³. (3) A ligand exchange takes place between $\equiv Ti(IV)$ –OH and H_2O_2 , yielding a new peroxide species, $\equiv Ti(IV)$ –OOH. This peroxide species is typically observed as a yellow compound

during the reaction $^{53-55}$. (4) Subsequently, $\equiv Ti(IV)-OOH$ undergoes decomposition to produce $^{\bullet}O_2^{-}$ radicals and regenerate $\equiv Ti(III)$ sites $^{55,\,56}$. The Ti(III) sites are fully recovered after this entire cycle. Furthermore, it's important to highlight that the reversible redox process, involving electron transfer between $\equiv Ti(III)$ and $\equiv Ti(IV)$, can occur at any point during the reaction. This phenomenon facilitates more efficient electron transfer, enhancing the Fenton-like reactivity. In the final step, the adsorbed AR molecule reacts with the generated ROS, ultimately transforming into the highly fluorescent product RF.

Our analyses clearly demonstrate that defect sites on TiO2 are responsible for the observed reactivity in AR oxidation. In turn, fluorogenic AR oxidation effectively correlates to the number of defect sites within a TiO2 NP. When combined with singlemolecule fluorescence imaging, one can chemically image the distribution of defect sites at the sub-nanoparticle level. As a demonstration, we employed single-molecule fluorescence microscopy (SMFM) and STORM-based super-resolution imaging to quantitatively map the defect site distributions within single TiO₂ NWs (Fig. 6a). Since the reaction is positively correlated to the defect contents, the localization of surfacegenerated RF molecules readily reflects the density and distribution of the defect sites (Fig. 6b). It is worth noting that the RF molecules do not reside on the TiO2 surface for long. Most of them desorb from the surface in tens of milliseconds after formation, resulting in the disappearance of the fluorescence signal under the microscope. Before they desorb, we utilized super-resolution imaging analysis to precisely determine the centroids of the emission signal at approximately 20 nm spatial resolution^{26-28, 57, 58} (Fig. 6c). The accumulation of all the RF centroids within an approximately 15 min reaction period reflects the density of defect sites along the nanowire. Notably, within each individual NW, the reactivity exhibited heterogeneity along its length (Fig. 6d and e). Furthermore, the reactivity varies from one NW to another, even when they share the same chemical composition and crystal phase (as illustrated in Fig. S3b and c). This reactivity heterogeneity, often concealed in ensemble measurements, poses a significant challenge. However, spatial catalysis mapping on single nanocatalysts offers a promising solution to this issue. Further analyses will be presented in our forthcoming research works.

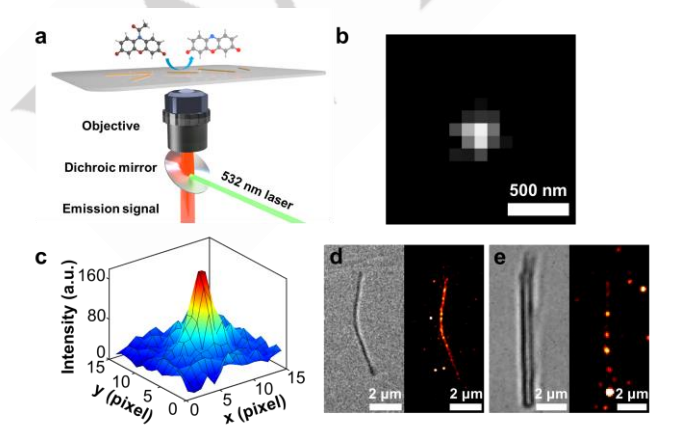


Figure 6. Single-molecule catalysis mapping along single TiO₂ NWs. (a) Experimental design of single-molecule catalysis

mapping, by using TIR fluorescence microscopy. (b) A typical fluorescence image of a single RF molecule. The emission of ${\rm TiO_2}$ NW was subtracted out. (c) Localizing an RF molecule in (b) by fitting its emission signal to a two-dimensional Gaussian function. The localization error is \pm 4.8 nm. (d, e) Correlation between the morphology of individual ${\rm TiO_2}$ NW captured by bright-field imaging (left), and super-resolution fluorescence imaging (right), reflecting the reactivity distributions. All experiments were performed with 1 μ M AR and 60 mM ${\rm H_2O_2}$ in 50 mM pH 7.4 phosphate buffer. 23483 (d) and 6442 (e) fluorescence bursts were collected.

Conclusion

In summary, we successfully synthesized TiO2 NPs with highly tunable catalytic reactivity for the AR oxidation. The structures and catalytic properties of these NPs were carefully tailored through controlled preparation conditions. Our comprehensive investigation unveiled that Ti(III) species are responsible for converting this fluorescence probe. The pH control during the hydrolysis step, thermal annealing, NaBH₄ reduction, and the existence of Magnéli's phase collectively suggest that the AR probe is sensitive to the Ti(III) content on TiO2 nanoparticles. Furthermore, the catalytic reactivity was inhibited by radical quenching reagents, shedding light on the presence of the concealed ROS, including •O₂⁻ and •OH radicals. Based on the catalytic analyses, we put forth a Fenton-like mechanism to elucidate the catalytic process on TiO2 NPs, wherein Ti(III) sites were found to recover after completing the reaction cycle. Additionally, our utilization of single-molecule catalysis mapping provided invaluable insights into the distribution of defect sites along individual TiO₂ NWs, which is challenging to attain through ensemble analyses. We envision that the application of singlemolecule methods can be extended to the field of heterogeneous catalysis, further aiding in the optimization of solid catalyst designs with enhanced reactivity.

Supporting Information

1. Materials.

Commercial TiO₂ NPs with rutile/anatase phase (CM-TiO₂, 634662), TiO₂ nanowires (TiO₂ NWs, ~100 nm × 10 μ m, 774510), TiCl₃ (10-15% basis, 14010), sodium hydroxide (NaOH, S5881), sodium borohydride (NaBH₄, 452882), p-benzoquinone (p-BQ, B10358) and tert-butanol (t-butanol, 471712) were purchased from Sigma-Aldrich. 30% hydrogen peroxide (H₂O₂, H1070) and 2.0 N hydrochloric acid (HCl, 18-603-172) were purchased from Spectrum Chemical Corp. The colloidal gold nanospheres (30 nm) were purchased from Nanopartz (A11-30-CIT-DIH). The fluorogenic probe, Amplex Red reagent (A12222), with a purity \geq 95%, was purchased from Invitrogen. Prior to single-molecule experiments, AR was dissolved in 50 mM, pH 7.4 phosphate buffer as the stock solution.

2. Synthesis and characterization of HM-TiO₂ NPs.

HM-TiO $_2$ NPs were synthesized by hydrothermal method^{59, 60}. Specifically, 20 mL of TiCl $_3$ stock solution was diluted with 400 mL DI-water and the homogeneous solution was heated to 60°C. Subsequently, 50% NaOH aqueous solution was dropped into the solution with intense stirring, until the pH reached 2.5 or 4.0, respectively. 2.0 N HCl solution was used to adjust the pH to desired value. The hydrolysis of TiCl $_3$ occurred which was indicated by the color change from purple to dark blue. Then, the dark blue precursor was kept at 60°C for 24 h. The composition is complex during the hydrothermal process. According to previous reports, we summarized the possible products to the best of our knowledge as shown in **Fig. S1**:

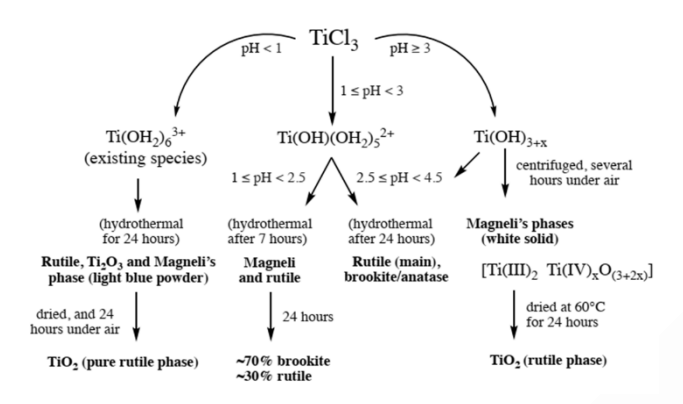


Figure S1. Diagram of the TiCl₃ hydrolysis at various pH values.

After cooling down to room temperature, the obtained sol was filtered, washed with DI-water twice and then dried at 110°C for 24 h. The sample was divided into several parts, and annealed at 300, 600 and 900°C for 24 h, respectively.

For the synthesis of reduced TiO_2 (R- TiO_2), 1 g of CM- TiO_2 (rutile/anatase mixture) was mixed with 200 mg of NaBH₄ (molar ratio of TiO_2 :NaBH₄ = 8:3), and the mixture was ground completely. The resulting mixture was heated under N₂ atmosphere to 300, 400 and 500°C, respectively, with a heating rate of 10°C min⁻¹, and kept for 30 min. The reduction followed the empirical equation 61-64:

$$8 \text{ TiO}_2 + \text{NaBH}_4 \rightarrow 8 \text{TiO}_{1.5} + \text{NaBO}_2 + 2 \text{H}_2 \text{O}$$

The stoichiometric ratio of TiO₂:NaBH₄ is 8:1. Thus, the amount of NaBH₄ was in excess. The obtained sample was then cooled down to room temperature and washed with DI-water to remove excess NaBH₄. The resulting black powder was presented as R-TiO₂-T (T for annealing temperature). A portion of the sample was then used in reverse oxidation under air atmosphere in a furnace for 1 h at 300, 600 and 900°C, respectively, at a rate of 20°C min⁻¹.

2.1. Thermogravimetric analysis and differential scanning calorimetry (TG-DSC).

The thermogravimetric analysis for HM-TiO $_2$ was conducted on a TA instrument TGA Q500 thermogravimetric analyzer. Approximately 50 mg of HM-TiO $_2$ powder was used in this

measurement. As shown in **Fig. S2**, there are three endothermic peaks for $HM-TiO_2$ prepared at pH 2.5 and 4.0.

The endothermic peak below 100°C belongs to the dehydration of fresh TiO_2 powder, while the peak around 200-300°C is attributed to partial crystalline transformation. Once the temperature is higher than 800°C, the crystal starts to transfer to rutile phase (the most stable crystalline phase). Thus, the annealing temperatures for HM- TiO_2 were set at 300, 600 and 900°C.

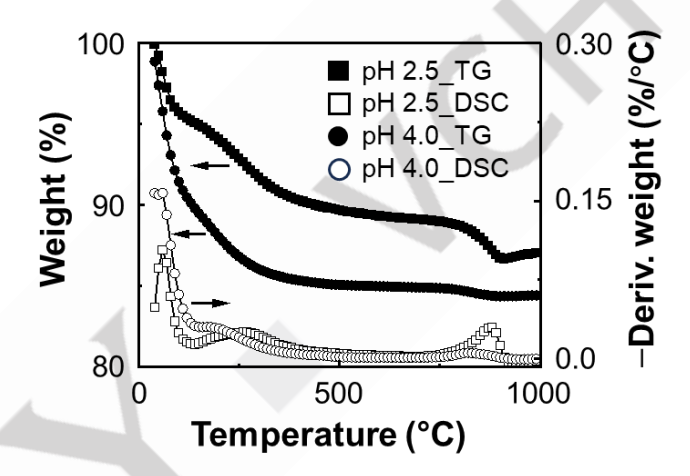


Figure S2. TG-DSC results of $HM-TiO_2$ prepared at pH 2.5 and 4.0.

2.2. Transmission electron microscopy (TEM).

All samples were dispersed in ethanol to the concentration of 10 $\mu g\ mL^{-1}$ for TEM imaging. Subsequently, 2 μL of the dispersed solution was drop-casted onto 200-mesh carbon-coated copper grid (Ted Pella, catalog #01840). The grids were dried in air for 2 h. The TEM and high-resolution TEM images were acquired using a Tecnai G2 F20 microscopy at an accelerating voltage of 200 kV.

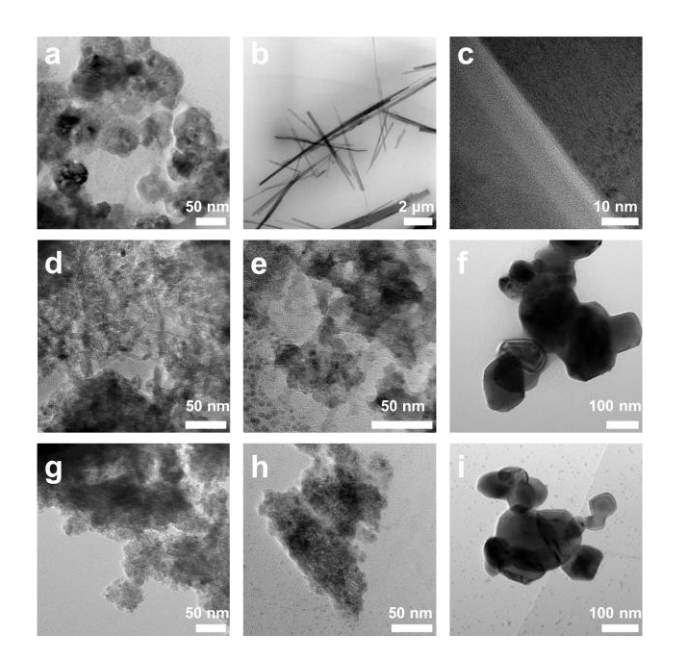


Figure S3. TEM images of C-TiO₂-R/A (a), TiO₂ NWs (b), high-resolution of TiO₂ NW (c), HM-TiO₂-2.5-110 (d), HM-TiO₂-2.5-300 (e), HM-TiO₂-2.5-900 (f), HM-TiO₂-4.0-110 (g), HM-TiO₂-4.0-300 (h), HM-TiO₂-4.0-900 (i).

The TEM images of TiO_2 NPs are shown in **Fig. S3**. It is observed that the fresh HM-TiO₂ NPs precipitated at pH 2.5 exhibited a rod-like morphology, while those precipitated at pH 4.0 exhibited clear morphological change. After annealing, the particles grew to a round shape and then sintered at 900°C. Besides, the high-resolution TEM image of TiO_2 NW reflected the lattice plane distance of ~0.32 nm, corresponding to the (1 1 0) facet of rutile phase.

2.3. X-ray diffraction (XRD).

Each sample was ground in a mortar and placed in the holder. XRD patterns of HM-TiO $_2$ NPs were recorded on a Rigaku MiniFlex X-ray diffractometer at 40 kV and 40 mA, using Cu K α radiation (λ = 1.5406 Å).

The crystalline structure of these prepared samples was analyzed, as shown in **Fig. S4**. The XRD patterns of commercial TiO_2 are presented for comparison. The strong diffraction peaks at 2θ = 27.4 and 36.1°, are assigned to the (1 1 0) and (1 0 1) planes, respectively, corresponding to the rutile phase (JCPDS 34-0180), while diffraction peaks at 25.3, 37.8, 48.0, 53.9, 55.1 and 62.7°, **Table S1**. Particle size of HM-TiO₂ and C-TiO₂.

are assigned to the (1 0 1), (0 0 4), (2 0 0), (1 0 5), (2 1 1) and (2 0 4) planes, respectively, for the anatase phase (JCPDS 21-1272). Thus, for fresh HM-TiO₂ sample prepared at pH 2.5, the dominant crystalline phase was rutile, while that for HM-TiO₂ prepared at pH 4.0 was anatase. Brookite phase was not observed in both samples. Interestingly, there are few peaks for sub-stoichiometric titanium oxides (Ti_xO_{2x-1}), known as Magneli phase, in the HM-TiO₂. The Magneli phase is reported to have relatively high reactivity^{30, 31}. However, it was not observed in commercial TiO₂. Further, the particle size was estimated by Scherrer's equation:

$$D = \frac{K\lambda}{\beta\cos\theta}$$

In which K is the dimensionless shape factor with a value close to unity, λ is the X-ray wavelength (1.5406 Å), β is the line broadening at half the maximum intensity (FWHM), and θ is the Bragg angle.

The estimated particle sizes summarized in **Table S1** are consistent with the size obtained from TEM images.

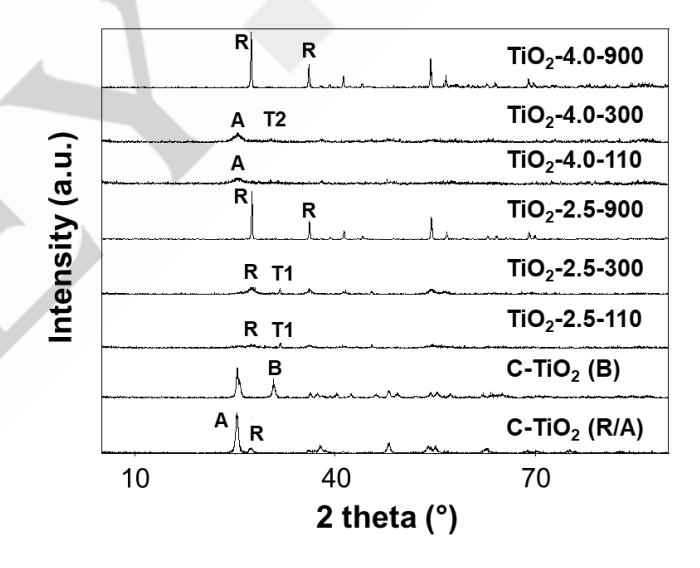


Figure S4. XRD patterns of HM-TiO₂ samples. Commercial TiO₂ is shown for comparison. R, A, B represent the crystalline phase of rutile, anatase and brookite, respectively. T_1 and T_2 represent the sub-stoichiometric titanium oxides, Ti_4O_7 and Ti_3O_5 , respectively.

Samples	C-TiO ₂ (R/A)	HM-TiO ₂ - 2.5-110	HM-TiO ₂ - 2.5-300	HM-TiO ₂ - 2.5-900	HM-TiO ₂ - 4.0-110	HM-TiO ₂ - 4.0-300	HM-TiO ₂ - 4.0-900
Size (nm)	14.5	n.d. ^a	7.2	60.9	n.d.ª	5.6	54.1

Note: (1 1 0) plane is used to the size estimation for rutile phase, while (1 0 1) plane is for anatase phase.

a: weak diffraction peaks due to the amorphous phase.

3. Fluorogenic probing reaction.

The N-deacetylation of AR oxidation, which is triggered by radicals²⁵, was used to probe the catalytic reactivity of HM-TiO₂ NPs. This reaction yields the highly fluorescent product RF at a 1:1 stoichiometric ratio, as shown in below equation:

The reactivity of TiO_2 NPs was confirmed by the time-dependent absorbance spectrum, which was obtained on Cary60 UV-Vis spectrometer. The formation of RFs is evidenced by increasing intensity of the absorbance peak at 571 nm (**Fig. S5a**).

To determine the reaction rates of HM-TiO $_2$ NPs, the ensemble catalysis was further performed by measuring the fluorescence spectra in an Agilent Cary60 fluorometer. Solutions of 19.4 μ M AR and 60 mM H $_2$ O $_2$ were pre-mixed in a 5 mM pH 7.4 phosphate buffer. The radical scavengers, p-BQ and t-butanol were mixed with the solution for the radical trapping experiments. To initiate the catalytic reaction, 0.5 mg of TiO $_2$ NPs were added to the reaction mixture. The formation of RF was indicated by increasing intensity of fluorescence signal at 583 nm (**Fig. 1a** in the main text). The AR to RF conversion is a pseudo-first order reaction; the fluorescence intensity increases linearly with the reaction time because of the relatively slow reaction rate (**Fig. S5b**). Hence, we used the slopes of the intensity-time trajectories for the calculation of reaction rates.

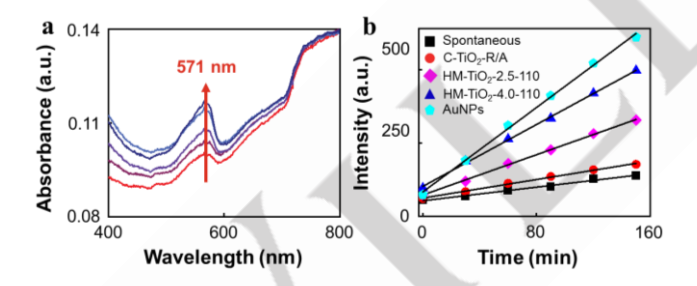


Figure S5. (a) In-situ absorbance spectra measurements of AR oxidation catalyzed by C-TiO₂. (b) The fluorescence intensities versus time from the measurements on C-TiO₂ (R/A represents the mixture of rutile and anatase) and HM-TiO₂ NPs. The catalytic reaction on 30 nm AuNPs (cyan symbol) is shown as a comparison. Reaction conditions: [AR] = $19.4 \, \mu$ M, [H₂O₂] = $60 \, \text{mM}$, [TiO₂ NPs] = $0.5 \, \text{mg mL}^{-1}$. [AuNPs] = $50 \, \text{pM}$. All experiments were performed in a 5 mM pH 7.4 phosphate buffer.

4. Single-molecule catalysis on single TiO_2 NWs.

Single-molecule catalysis experiments were performed on an objective-type total internal reflection (TIR) fluorescence microscope (Olympus IX83) inside a microfluidic chamber. Approximately 50 μ L of 5 μ g mL⁻¹ TiO₂ NWs ethanol solution was spin-casted onto a coverslip for the optimal nanoparticle

dispersion. Subsequently, the coverslip was assembled onto a flow chamber, following the protocols outlined in our prior work 55 . Once the chamber was mounted under the microscope, single $\rm TiO_2~NWs~were~identified~through~bright~field~imaging.$ Subsequently, premixed reactant solution (1 μM AR, 60 mM $\rm H_2O_2$ and 50 mM pH 7.4 phosphate buffer) was supplied via a syringe pump (Genie Touch, Kent Scientific) at the rate of 20 μL min $^{-1}$ throughout the measurement.

To excite the fluorescence emission, we focused a 532 nm continuous-wave laser (DragonLaser) onto a 35 × 35 μm^2 area within the microfluidic cell. It is worth mentioning that although TiO₂ exhibits photochemical activities, the 532 nm laser does not trigger the AR conversion, as demonstrated in our previous work 65 . The emission signals of RF were collected by a 100x NA 1.49 oil immersion objective lens (UAPON 100xOTIRF, Olympus), filtered by a longpass filter (Chroma, ET542lp) and a bandpass filter (Chroma ET575/50m), and captured by a sCMOS camera (Photometrics Prime 95B) at a frame rate of 50 ms.

To obtain the catalysis mapping of the product RF molecules along single TiO2 NWs, the analysis included the following major steps: (1) Capture the bright-field image for single TiO₂ NWs. (2) In the same field of view, record the fluorescence signals at a given reaction condition ([AR] = 1 μ M, [H₂O₂] = 60 mM). (3) Identify single RF molecules in each frame and fit their emission signals Gaussian function: $PSF_G(x, y|\theta) =$ $\frac{\theta_{\rm N}}{2\pi\theta_{\sigma}^2} \exp\left(-\frac{(x-\theta_{\rm X})^2+\left(y-\theta_{\rm y}\right)^2}{2\theta_{\sigma}^2}\right) + \; \theta_{\rm b} \; . \; \; {\rm Here} \; \; \theta_{\rm b} \; \; {\rm is} \; \; {\rm the} \; \; {\rm background}$ fluorescence level, θ_{σ} is the imaged size of the molecule, θ_{x} and θ_{v} are the sub-pixel molecular coordinates and PSF_G gives the expected photon count at the integer pixel position $(x, y)^{66}$. The fitted results were further filtered using the uncertainties (3 nm ~ 38 nm) and σ value (30 nm ~ 500 nm) because the filtered fluorescence events were unlikely from single fluorophores according to the previous studies⁵⁸⁻⁶¹. In addition, we applied an intensity filter (< 800 counts) to remove the intense noise signals from the output results. Thus, the accurate position of a single RF molecule in sub-pixel resolution was extracted. (4) Correlate the bright-field images of each TiO2 NW with the positions of its catalytic product RF molecules from single-molecule fluorescence imaging.

Acknowledgments

The authors thank Kent State University's Farris Family Innovation Award for financial support. H.S. acknowledges the National Science Foundation (NSF) (No. CHE2247709) for grant support.

Keywords: titanium dioxide • defect site • chemical oxidation • fluorogenic probe • single-molecule catalysis

Reference

- (1) Bai, Y.; Mora-Sero, I.; De Angelis, F.; Bisquert, J.; Wang, P. Titanium dioxide nanomaterials for photovoltaic applications. *Chem. Rev.* **2014**, *114* (19), 10095-10130. DOI: 10.1021/cr400606n From NLM PubMed-not-MEDLINE.
- (2) Kang, X.; Liu, S.; Dai, Z.; He, Y.; Song, X.; Tan, Z. Titanium Dioxide: From Engineering to Applications. *Catalysts* **2019**, 9 (2). DOI: 10.3390/catal9020191.
- (3) G. Ertl, H. K., J. Weitkamp. Handbook of Heterogeneous Catalysis *VCH* **1997**.
- (4) A. Fujishima, K. H. Electrochemical Photolysis of Water at a Semiconductor Electrode. *Nature* **1972**, *238* (7), 37-38.
- (5) D.A. Tryk, A. F., K. Honda. Recent topics in photoelectrochemistry: achievements and future prospects. *Electrochim. Acta* **2000**, *45*, 2363-2376
- Electrochim. Acta **2000**, 45, 2363-2376.

 (6) Banerjee, S.; Pillai, S. C.; Falaras, P.; O'Shea, K. E.; Byrne, J. A.; Dionysiou, D. D. New Insights into the Mechanism of Visible Light Photocatalysis. *J. Phys. Chem. Lett.* **2014**, 5 (15), 2543-2554. DOI: 10.1021/jz501030x From NLM PubMed-not-MEDLINE.
- (7) Dette, C.; Perez-Osorio, M. A.; Kley, C. S.; Punke, P.; Patrick, C. E.; Jacobson, P.; Giustino, F.; Jung, S. J.; Kern, K. TiO_2 anatase with a bandgap in the visible region. *Nano Lett* **2014**, *14* (11), 6533-6538. DOI: 10.1021/nl503131s From NLM Medline.
- (8) Jang, Y. H.; Jang, Y. J.; Kim, S.; Quan, L. N.; Chung, K.; Kim, D. H. Plasmonic Solar Cells: From Rational Design to Mechanism Overview. *Chem Rev* **2016**, *116* (24), 14982-15034. DOI:
- 10.1021/acs.chemrev.6b00302 From NLM PubMed-not-MEDLINE. (9) Nowotny, J.; Alim, M. A.; Bak, T.; Idris, M. A.; Ionescu, M.; Prince, K.; Sahdan, M. Z.; Sopian, K.; Mat Teridi, M. A.; Sigmund, W. Defect chemistry and defect engineering of TiO₂-based semiconductors for solar energy conversion. *Chem. Soc. Rev.* **2015**, 44 (23), 8424-8442. DOI: 10.1039/c4cs00469h From NLM
- (10) Gao, C.; Meng, Q.; Zhao, K.; Yin, H.; Wang, D.; Guo, J.; Zhao, S.; Chang, L.; He, M.; Li, Q.; et al. Co₃O₄ Hexagonal Platelets with Controllable Facets Enabling Highly Efficient Visible-Light Photocatalytic Reduction of CO₂. *Adv. Mater.* **2016**, *28* (30), 6485-6490. DOI: 10.1002/adma.201601387 From NLM PubMed-not-MEDLINE.

PubMed-not-MEDLINE.

- (11) Jiang, L.; Liu, K.; Hung, S. F.; Zhou, L.; Qin, R.; Zhang, Q.; Liu, P.; Gu, L.; Chen, H. M.; Fu, G.; et al. Facet engineering accelerates spillover hydrogenation on highly diluted metal nanocatalysts. *Nat. Nanotechnol.* **2020**, *15* (10), 848-853. DOI: 10.1038/s41565-020-0746-x From NLM PubMed-not-MEDLINE.
- (12) Zhang, Y.; Liu, J. X.; Qian, K.; Jia, A.; Li, D.; Shi, L.; Hu, J.; Zhu, J.; Huang, W. Structure Sensitivity of Au-TiO₂ Strong Metal-Support Interactions. *Angew. Chem. Int. Ed.* **2021**, *60* (21), 12074-12081. DOI: 10.1002/anie.202101928 From NLM PubMed-not-MEDLINE. (13) Hou, Q.; Cai, J.; Zuo, L.; Chen, H.; Fu, Y.; Shen, J. Selective hydrogenation of furfural over supported nickel and nickel phosphide catalysts. *Appl. Surf. Sci.* **2023**, *619* (15). DOI:
- 10.1016/j.apsusc.2023.156738. (14) Cai, J.; Zuo, L.; Hao, C.; Fu, Y.; Shen, J. Effect of Ethylamines on the Hydrogenation of Toluene over Supported Nickel Catalysts. *Ind. Eng. Chem. Res.* **2018**, *57* (45), 15262-15267. DOI: 10.1021/acs.iecr.8b02565.
- (15) Zuo, L.; Cai, J.; Yang, C.; Hao, C.; Fu, Y.; Shen, J. Highly Loaded and Dispersed Cobalt Catalysts for the Hydrogenation of Toluene with Triethylamine. *Ind. Eng. Chem. Res.* **2019**, *58* (42), 19456-19464. DOI: 10.1021/acs.iecr.9b03851.
- (16) Kumaravel, V.; Mathew, S.; Bartlett, J.; Pillai, S. C. Photocatalytic hydrogen production using metal doped TiO₂: A review of recent advances. *Appl. Catal. B* **2019**, *244*, 1021-1064. DOI: 10.1016/j.apcatb.2018.11.080.
- (17) Pei, D. N.; Gong, L.; Zhang, A. Y.; Zhang, X.; Chen, J. J.; Mu, Y.; Yu, H. Q. Defective titanium dioxide single crystals exposed by high-energy 001 facets for efficient oxygen reduction. *Nat. Commun.* **2015**, *6*, 8696. DOI: 10.1038/ncomms9696 From NLM PubMed-not-MEDLINE.
- (18) Ong, W. J.; Tan, L. L.; Chai, S. P.; Yong, S. T.; Mohamed, A. R. Facet-dependent photocatalytic properties of TiO₂ -based composites for energy conversion and environmental remediation. *ChemSusChem* **2014**, 7 (3), 690-719. DOI: 10.1002/cssc.201300924 From NLM Medline.
- (19) Pan, X.; Yang, M. Q.; Fu, X.; Zhang, N.; Xu, Y. J. Defective TiO_2 with oxygen vacancies: synthesis, properties and photocatalytic

- applications. *Nanoscale* **2013**, *5* (9), 3601-3614. DOI: 10.1039/c3nr00476g From NLM PubMed-not-MEDLINE. (20) Zuo, L.; Hossain, M. A.; Pokhrel, B.; Chang, W.-S.; Shen, H. Catalysis driven by biohybrid nanozyme. *Advanced Sensor and Energy Materials* **2022**, *1* (3). DOI: 10.1016/j.asems.2022.100024. (21) Martin Setvín, U. A., Philipp Scheiber, YeFei Li, Weiyi Hou, Michael Schmid, Annabella Selloni, Ulrike Diebold. Reaction of O₂ with Subsurface Oxygen Vacancies on TiO₂ Anatase (101). *Science* **2013**, *341* (30), 988-991.
- (22) Zuo, L.; Cai, J.; Guo, Z.; Fu, Y.; Shen, J. Effect of amine group on the hydrogenation of aromatic rings over Ru/MgO-Al2O3 catalysts. *Catal Commun* **2022**, *170*. DOI: 10.1016/j.catcom.2022.106496.
- (23) Lu, Q.; Peng, W.; Xun, S.; He, M.; Ma, R.; Jiang, W.; Zhu, W.; Li, H. Controllable preparation of highly dispersed TiO₂ nanoparticles for enhanced catalytic oxidation of dibenzothiophene in fuels. *Appl. Organomet. Chem.* **2018**, 32 (6). DOI: 10.1002/aoc.4351.
- (24) Sánchez, L. D.; Taxt-Lamolle, S. F. M.; Hole, E. O.; Krivokapić, A.; Sagstuen, E.; Haugen, H. J. TiO₂ suspension exposed to H₂O₂ in ambient light or darkness: Degradation of methylene blue and EPR evidence for radical oxygen species. *Appl. Catal. B* **2013**, *142-143*, 662-667. DOI: 10.1016/j.apcatb.2013.05.017.
- (25) Debski, D.; Smulik, R.; Zielonka, J.; Michalowski, B.; Jakubowska, M.; Debowska, K.; Adamus, J.; Marcinek, A.; Kalyanaraman, B.; Sikora, A. Mechanism of oxidative conversion of Amplex(R) Red to resorufin: Pulse radiolysis and enzymatic studies. *Free Radic. Biol.* **2016**, *95*, 323-332. DOI:
- 10.1016/j.freeradbiomed.2016.03.027 From NLM Medline. (26) Sambur, J. B.; Chen, T.-Y.; Choudhary, E.; Chen, G.; Nissen, E. J.; Thomas, E. M.; Zou, N.; Chen, P. Sub-particle reaction and photocurrent mapping to optimize catalyst-modified photoanodes. *Nature* **2016**, *530* (7588), 77-80. DOI: 10.1038/nature16534.
- (27) Shen, M.; Ding, T.; Hartman, S. T.; Wang, F.; Krucylak, C.; Wang, Z.; Tan, C.; Yin, B.; Mishra, R.; Lew, M. D.; et al. Nanoscale Colocalization of Fluorogenic Probes Reveals the Role of Oxygen Vacancies in the Photocatalytic Activity of Tungsten Oxide Nanowires. *ACS Catalysis* **2020**, *10* (3), 2088-2099. DOI: 10.1021/acscatal.9b04481.
- (28) Huang, T.-X.; Dong, B.; Filbrun, S. L.; Okmi, A. A.; Cheng, X.; Yang, M.; Mansour, N.; Lei, S.; Fang, N. Single-molecule photocatalytic dynamics at individual defects in two-dimensional layered materials. *Science Advances* 7 (40), eabj4452. DOI: 10.1126/sciadv.abj4452 (acccessed 2024/04/11).
- (29) Golub, E.; Freeman, R.; Willner, I. Hemin/G-quadruplex-catalyzed aerobic oxidation of thiols to disulfides: application of the process for the development of sensors and aptasensors and for probing acetylcholine esterase activity. *Anal. Chem* **2013**, *85* (24), 12126-12133. DOI: 10.1021/ac403305k From NLM Medline. (30) Geng, P.; Su, J.; Miles, C.; Comninellis, C.; Chen, G. Highly-Ordered Magnéli Ti₄O₇ Nanotube Arrays as Effective Anodic Material for Electro-oxidation. *Electrochim. Acta* **2015**, *153*, 316-324. DOI: 10.1016/j.electacta.2014.11.178.
- (31) Toyoda, M.; Yano, T.; Tryba, B.; Mozia, S.; Tsumura, T.; Inagaki, M. Preparation of carbon-coated Magneli phases Ti_nO_{2n-1} and their photocatalytic activity under visible light. *Appl. Catal. B* **2009**, *88* (1-2), 160-164. DOI: 10.1016/j.apcatb.2008.09.009. (32) Walsh, F. C.; Wills, R. G. A. The continuing development of Magnéli phase titanium sub-oxides and Ebonex® electrodes. *Electrochim. Acta* **2010**, *55* (22), 6342-6351. DOI: 10.1016/j.electacta.2010.05.011.
- (33) Chen, X.; Liu, L.; Huang, F. Black titanium dioxide (TiO₂) nanomaterials. *Chem. Soc. Rev.* **2015**, *44* (7), 1861-1885. DOI: 10.1039/c4cs00330f From NLM PubMed-not-MEDLINE. (34) Wang, Z.; Yang, C.; Lin, T.; Yin, H.; Chen, P.; Wan, D.; Xu, F.; Huang, F.; Lin, J.; Xie, X.; et al. H-Doped Black Titania with Very High Solar Absorption and Excellent Photocatalysis Enhanced by Localized Surface Plasmon Resonance. *Adv Funct Mater* **2013**, *23* (43), 5444-5450. DOI: 10.1002/adfm.201300486.
- (35) Xu, J.; Zhang, J.; Cai, Z.; Huang, H.; Huang, T.; Wang, P.; Wang, X. Facile and Large-scale Synthesis of Defective Black TiO_{2-x}(B) Nanosheets for Efficient Visible-light-driven Photocatalytic Hydrogen Evolution. *Catalysts* **2019**, 9 (12). DOI: 10.3390/catal9121048.
- (36) Schneider, J. T.; Firak, D. S.; Ribeiro, R. R.; Peralta-Zamora, P. Use of scavenger agents in heterogeneous photocatalysis: truths,

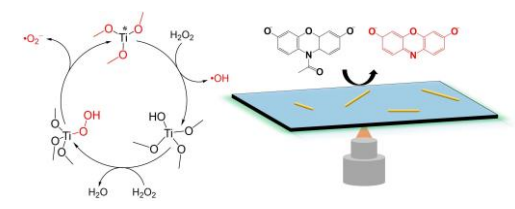
- half-truths, and misinterpretations. *Phys. Chem. Chem. Phys.* **2020**, 22 (27), 15723-15733. DOI: 10.1039/d0cp02411b From NLM PubMed-not-MEDLINE.
- (37) Mohammad Malakootian, A. N. a. M. A. G. Photocatalytic degradation of ciprofloxacin antibiotic by TiO_2 nanoparticles immobilized on a glass plate. *Chem Eng Commun* **2020**, *207* (1), 56-72. DOI: 10.1080/00986445.2019.1573168.
- (38) Liu, K.; Cao, M.; Fujishima, A.; Jiang, L. Bio-inspired titanium dioxide materials with special wettability and their applications. *Chem. Rev.* **2014**, *114* (19), 10044-10094. DOI: 10.1021/cr4006796 From NLM Medline.
- (39) Miao, F.; Liu, Y.; Gao, M.; Yu, X.; Xiao, P.; Wang, M.; Wang, S.; Wang, X. Degradation of polyvinyl chloride microplastics via an electro-Fenton-like system with a TiO₂/graphite cathode. *J. Hazard. Mater.* **2020**, 399, 123023. DOI: 10.1016/j.jhazmat.2020.123023 From NLM PubMed-not-MEDLINE.
- (40) Wang, D.; Wu, H.; Wang, C.; Gu, L.; Chen, H.; Jana, D.; Feng, L.; Liu, J.; Wang, X.; Xu, P.; et al. Self-Assembled Single-Site Nanozyme for Tumor-Specific Amplified Cascade Enzymatic Therapy. *Angew. Chem. Int. Ed.* **2021**, *60* (6), 3001-3007. DOI: 10.1002/anie.202008868 From NLM Medline.
- (41) Ha, J. W.; Ruberu, T. P. A.; Han, R.; Dong, B.; Vela, J.; Fang, N. Super-Resolution Mapping of Photogenerated Electron and Hole Separation in Single Metal—Semiconductor Nanocatalysts. *Journal of the American Chemical Society* **2014**, *136* (4), 1398-1408. DOI: 10.1021/ja409011y.
- (42) Liu, Y.; Zhang, K.; Tian, X.; Zhou, L.; Liu, J.; Liu, B. Quantitative Single-Particle Fluorescence Imaging Elucidates Semiconductor Shell Influence on Ag@TiO2 Photocatalysis. *ACS Applied Materials & Interfaces* **2021**, *13* (6), 7680-7687. DOI: 10.1021/acsami.0c18508.
- (43) An, J.; Song, X.; Wan, W.; Chen, Y.; Si, H.; Duan, H.; Li, L.; Tang, B. Kinetics of the Photoelectron-Transfer Process Characterized by Real-Time Single-Molecule Fluorescence Imaging on Individual Photocatalyst Particles. *ACS Catalysis* **2021**, *11* (12), 6872-6882. DOI: 10.1021/acscatal.1c00983.
- (44) Wu, S.; Lee, J.-K.; Lim, P. C.; Xu, R.; Zhang, Z. Superresolution imaging of photogenerated charges on CdS/g-C3N4 heterojunctions and its correlation with photoactivity. *Nanoscale* **2022**, *14* (14), 5612-5624, 10.1039/D2NR00316C. DOI: 10.1039/D2NR00316C.
- (45) Xu, W.; Jain, P. K.; Beberwyck, B. J.; Alivisatos, A. P. Probing Redox Photocatalysis of Trapped Electrons and Holes on Single Sbdoped Titania Nanorod Surfaces. *Journal of the American Chemical Society* **2012**, *134* (9), 3946-3949. DOI: 10.1021/ja210010k.

 (46) Mao, X.; Liu, C.; Hesari, M.; Zou, N.; Chen, P. Super-resolution imaging of non-fluorescent reactions via competition. *Nature Chemistry* **2019**, *11* (8), 687-694. DOI: 10.1038/s41557-019-0288-8.

 (47) Wang, W.-K.; Chen, J.-J.; Lou, Z.-Z.; Kim, S.; Fujitsuka, M.; Yu, H.-Q.; Majima, T. Single-molecule and -particle probing crystal edge/corner as highly efficient photocatalytic sites on a single TiO2 particle. *Proceedings of the National Academy of Sciences* **2019**, *116* (38), 18827-18833. DOI: 10.1073/pnas.1907122116 (acccessed 2024/04/11)
- (48) Lousada, C. M.; Brinck, T.; Jonsson, M. Application of reactivity descriptors to the catalytic decomposition of hydrogen peroxide at oxide surfaces. *Comput. Theor. Chem.* **2015**, *1070*, 108-116. DOI: 10.1016/j.comptc.2015.08.001.
- (49) Buchalska, M.; Kobielusz, M.; Matuszek, A.; Pacia, M.; Wojtyła, S.; Macyk, W. On Oxygen Activation at Rutile- and Anatase-TiO₂. *ACS Catal* **2015**, *5* (12), 7424-7431. DOI: 10.1021/acscatal.5b01562.
- (50) Lousada, C. M.; Johansson, A. J.; Brinck, T.; Jonsson, M. Mechanism of H_2O_2 Decomposition on Transition Metal Oxide Surfaces. *J. Phys. Chem. C* **2012**, *116* (17), 9533-9543. DOI: 10.1021/jp300255h.
- (51) Lousada, C. M.; Johansson, A. J.; Brinck, T.; Jonsson, M. Reactivity of metal oxide clusters with hydrogen peroxide and water-a DFT study evaluating the performance of different exchange-correlation functionals. *Phys. Chem. Chem. Phys.* **2013**, *15* (15), 5539-5552. DOI: 10.1039/c3cp44559c From NLM Medline. (52) Heck, K. N.; Wang, Y.; Wu, G.; Wang, F.; Tsai, A. L.; Adamson, D. T.; Wong, M. S. Effectiveness of metal oxide catalysts for the degradation of 1,4-dioxane. *RSC Adv.* **2019**, *9* (46), 27042-27049. DOI: 10.1039/c9ra05007h From NLM PubMed-not-MEDLINE.

- (53) Barsukov, D. V.; Pershin, A. N.; Subbotina, I. R. Increase of CO photocatalytic oxidation rate over anatase TiO₂ particles by adsorbed water at moderate coverages: The role of peroxide species. *J. Photochem. Photobiol. A* **2016**, *324*, 175-183. DOI: 10.1016/j.jphotochem.2016.03.021.
- (54) Ryuhei Nakamura, A. I., Kei Murakoshi, and Yoshihiro Nakato. In Situ FTIR Studies of Primary Intermediates of Photocatalytic Reactions on Nanocrystalline TiO₂ Films in Contact with Aqueous Solutions. *J. Am. Chem. Soc.* **2003**, *125* (24), 7443-7450. (55) Rahemi, V.; Trashin, S.; Hafideddine, Z.; Meynen, V.; Van Doorslaer, S.; De Wael, K. Enzymatic sensor for phenols based on titanium dioxide generating surface confined ROS after treatment with H₂O₂. *Sens. Actuators B Chem.* **2019**, *283*, 343-348. DOI: 10.1016/j.snb.2018.12.039.
- (56) Qi Zhao, X.-h. B., Yi Wang, Li-wu Lin, Gang Li, Xin-wen Guo, and Xiang-sheng Wang. Studies on superoxide O₂⁻ species on the interaction of TS-1 zeolite with H₂O₂. *J. Mol. Catal. A Chem.* **2000**, *157*, 265-268.
- (57) Andoy, N. M.; Zhou, X.; Choudhary, E.; Shen, H.; Liu, G.; Chen, P. Single-molecule catalysis mapping quantifies site-specific activity and uncovers radial activity gradient on single 2D nanocrystals. *J. Am. Chem. Soc.* **2013**, *135* (5), 1845-1852. DOI: 10.1021/ja309948y From NLM Medline.
- (58) Zhou, X.; Andoy, N. M.; Liu, G.; Choudhary, E.; Han, K. S.; Shen, H.; Chen, P. Quantitative super-resolution imaging uncovers reactivity patterns on single nanocatalysts. *Nat. Nanotechnol.* **2012**, 7 (4), 237-241. DOI: 10.1038/nnano.2012.18 From NLM Medline. (59) Li, J.-G.; Ishigaki, T.; Sun, X. Anatase, Brookite, and Rutile Nanocrystals via Redox Reactions under Mild Hydrothermal Conditions: Phase-Selective Synthesis and Physicochemical Properties. *The Journal of Physical Chemistry C* **2007**, *111* (13), 4969-4976. DOI: 10.1021/jp0673258.
- (60) Noman, M. T.; Ashraf, M. A.; Ali, A. Synthesis and applications of nano-TiO2: a review. *Environmental Science and Pollution Research* **2019**, *26* (4), 3262-3291. DOI: 10.1007/s11356-018-3884-
- (61) Liu, S.; Bao, L.; Jia, Q.; Qiao, X.; Wang, D. Controllable preparation of black titanium dioxide and its wave-absorbing properties. *Applied Physics A* **2023**, *129* (2), 119. DOI: 10.1007/s00339-022-06301-6.
- (62) Saensook, S.; Sirisuk, A. A factorial experimental design approach to obtain defect-rich black TiO2 for photocatalytic dye degradation. *Journal of Water Process Engineering* **2022**, *45*, 102495. DOI: https://doi.org/10.1016/j.jwpe.2021.102495.
- (63) Andronic, L.; Ghica, D.; Stefan, M.; Mihalcea, C. G.; Vlaicu, A.-M.; Karazhanov, S. Visible-Light-Active Black TiO2 Nanoparticles with Efficient Photocatalytic Performance for Degradation of Pharmaceuticals. In *Nanomaterials*, 2022; Vol. 12.
- (64) Sun, L.; Li, Z.; Li, Z.; Hu, Y.; Chen, C.; Yang, C.; Du, B.; Sun, Y.; Besenbacher, F.; Yu, M. Design and mechanism of core–shell TiO2 nanoparticles as a high-performance photothermal agent. *Nanoscale* **2017**, *9* (42), 16183-16192, 10.1039/C7NR02848B. DOI: 10.1039/C7NR02848B.
- (65) Zuo, L.; King, H.; Hossain, M. A.; Farhana, F.; Kist, M. M.; Stratton, R. L.; Chen, J.; Shen, H. Single-Molecule Spectroscopy Reveals the Plasmon-Assisted Nanozyme Catalysis on AuNR@TiO₂. Chemical & Biomedical Imaging 2023. DOI: 10.1021/cbmi.3c00096.
- (66) Ovesný, M.; Křížek, P.; Borkovec, J.; Švindrych, Z.; Hagen, G. M. ThunderSTORM: a comprehensive ImageJ plug-in for PALM and STORM data analysis and super-resolution imaging. *Bioinformatics* **2014**, *30* (16), 2389-2390. DOI: 10.1093/bioinformatics/btu202 (accessed 4/9/2024).

Entry for the Table of Contents



Defect site-rich titanium dioxide promote the activation of hydrogen peroxide generating more reactive oxidative species and exhibit outstanding advantages on chemical oxidation. The cycle of Ti(III) and Ti(IV) plays an important role in the catalytic enhancement. More importantly, single-molecule catalysis has great potential to avoid the heterogeneity of nanocatalysts and probe the defect site distributions.

